

# The very large n2EDM magnetically shielded room with an exceptional performance for fundamental physics measurements

Cite as: Rev. Sci. Instrum. **93**, 095105 (2022); <https://doi.org/10.1063/5.0101391>

Submitted: 31 May 2022 • Accepted: 19 August 2022 • Published Online: 29 September 2022

N. J. Ayres, G. Ban,  G. Bison, et al.



View Online



Export Citation



CrossMark

## ARTICLES YOU MAY BE INTERESTED IN

[Hard x-ray spectrometer calibrations using a portable#120#kV x-ray source](#)



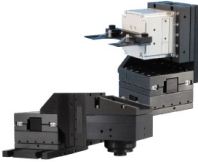
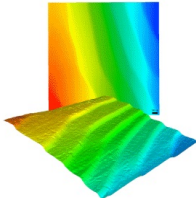
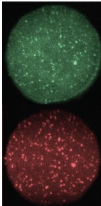
Review of Scientific Instruments **93**, 093529 (2022); <https://doi.org/10.1063/5.0099178>

[AC compensation of 3D magnetic diagnostic signals in DIII-D and National Spherical Torus Experiment-Upgrade \(NSTX-U\) for real-time application](#)

Review of Scientific Instruments **93**, 093528 (2022); <https://doi.org/10.1063/5.0101630>

[Improved electron trajectory and power distribution in APPLE-knot undulator](#)

Review of Scientific Instruments **93**, 093905 (2022); <https://doi.org/10.1063/5.0081034>

	<p>Nanopositioning Systems</p> 	<p>Modular Motion Control</p> 	<p>AFM and NSOM Instruments</p> 	<p>Single Molecule Microscopes</p> 
---	--	--	---	--

# The very large n2EDM magnetically shielded room with an exceptional performance for fundamental physics measurements

Cite as: *Rev. Sci. Instrum.* **93**, 095105 (2022); doi: [10.1063/5.0101391](https://doi.org/10.1063/5.0101391)

Submitted: 31 May 2022 • Accepted: 19 August 2022 •

Published Online: 29 September 2022

















View Online



Export Citation



CrossMark

N. J. Ayres,<sup>1</sup> G. Ban,<sup>2</sup> G. Bison,<sup>3,a)</sup>  K. Bodek,<sup>4</sup> V. Bondar,<sup>1</sup> T. Bouillaud,<sup>5</sup> B. Clement,<sup>5</sup>   
E. Chanel,<sup>6,b)</sup> P.-J. Chiu,<sup>3,c)</sup> C. B. Crawford,<sup>7</sup> M. Daum,<sup>3</sup> C. B. Doorenbos,<sup>3,c)</sup> S. Emmenegger,<sup>1</sup>  
A. Fratangelo,<sup>6</sup>  M. Fertl,<sup>8</sup>  W. C. Griffith,<sup>9</sup>  Z. D. Grujic,<sup>10</sup>  P. G. Harris,<sup>9</sup>  K. Kirch,<sup>1</sup> J. Krempel,<sup>1</sup>  
B. Lauss,<sup>3,a)</sup>  T. Lefort,<sup>2</sup> O. Naviliat-Cuncic,<sup>2</sup>  D. Pais,<sup>3</sup> F. M. Piegsa,<sup>6</sup> G. Pignol,<sup>5</sup> G. Rauscher,<sup>11</sup>  
D. Rebreyend,<sup>5</sup> I. Rienäcker,<sup>3,c)</sup> D. Ries,<sup>12</sup> S. Roccia,<sup>5</sup> D. Rozpedzik,<sup>4</sup> W. Saenz-Arevalo,<sup>2</sup>  
P. Schmidt-Wellenburg,<sup>3</sup> A. Schnabel,<sup>13</sup>  N. Severijns,<sup>14</sup>  B. Shen,<sup>12</sup> M. Staab,<sup>11</sup> K. Svirina,<sup>5</sup>   
R. Tavakoli Dinani,<sup>14</sup> J. Thorne,<sup>6</sup> N. Yazdandoost,<sup>12</sup>  J. Zejma,<sup>4</sup>  G. Zsigmond,<sup>3</sup>  
and nEDM Collaboration

## AFFILIATIONS

<sup>1</sup>Institute for Particle Physics and Astrophysics, ETH Zürich, CH-8093 Zurich, Switzerland

<sup>2</sup>Normandie Université, ENSICAEN, UNICAEN, CNRS/IN2P3, LPC Caen, 14000 Caen, France

<sup>3</sup>Paul Scherrer Institut, CH-5232 Villigen PSI, Switzerland

<sup>4</sup>Marian Smoluchowski Institute of Physics, Jagiellonian University, 30-348 Cracow, Poland

<sup>5</sup>Université Grenoble Alpes, CNRS, Grenoble INP, LPSC-IN2P3, 38026 Grenoble, France

<sup>6</sup>Laboratory for High Energy Physics and Albert Einstein Center for Fundamental Physics, University of Bern, CH-3012 Bern, Switzerland

<sup>7</sup>Department of Physics and Astronomy, University of Kentucky, Lexington, Kentucky 40506, USA

<sup>8</sup>Institute of Physics, Johannes Gutenberg University, D-55128 Mainz, Germany

<sup>9</sup>Department of Physics and Astronomy, University of Sussex, Falmer, Brighton BN1 9QH, United Kingdom

<sup>10</sup>Institute of Physics, Photonics Center, University of Belgrade, 11080 Belgrade, Serbia

<sup>11</sup>VAC-Vacuumschmelze, Grüner Weg 37, 63450 Hanau, Germany

<sup>12</sup>Department of Chemistry–TRIGA Site, Johannes Gutenberg University Mainz, D-55128 Mainz, Germany

<sup>13</sup>Physikalisch-Technische Bundesanstalt, Abbestr. 2-12, D-10587 Berlin, Germany

<sup>14</sup>Instituut voor Kern-en Stralingsfysica, University of Leuven, B-3001 Leuven, Belgium

<sup>a)</sup> Authors to whom correspondence should be addressed: [georg.bison@psi.ch](mailto:georg.bison@psi.ch) and [bernhard.lauss@psi.ch](mailto:bernhard.lauss@psi.ch)

<sup>b)</sup> Current address: Institut-Langevin, Grenoble, France.

<sup>c)</sup> Also at: ETH Zürich, Zurich, Switzerland.

## ABSTRACT

We present the magnetically shielded room (MSR) for the n2EDM experiment at the Paul Scherrer Institute, which features an interior cubic volume with each side of length 2.92 m, thus providing an accessible space of 25 m<sup>3</sup>. The MSR has 87 openings of diameter up to 220 mm for operating the experimental apparatus inside and an intermediate space between the layers for housing sensitive signal processing electronics. The characterization measurements show a remanent magnetic field in the central 1 m<sup>3</sup> below 100 pT and a field below 600 pT in the entire inner volume, up to 4 cm to the walls. The quasi-static shielding factor at 0.01 Hz measured with

a sinusoidal 2  $\mu\text{T}$  peak-to-peak signal is about 100 000 in all three spatial directions and increases rapidly with frequency to reach  $10^8$  above 1 Hz.

© 2022 Author(s). All article content, except where otherwise noted, is licensed under a Creative Commons Attribution (CC BY) license (<http://creativecommons.org/licenses/by/4.0/>). <https://doi.org/10.1063/5.0101391>

## I. INTRODUCTION

Magnetic shielding is used when the absolute magnetic field strength at a measurement site must be lower than the Earth's magnetic field or when Earth's or ambient magnetic field fluctuations would limit the measurement accuracy.

A commonly used parameter to describe the performance of shields is their shielding factor. It is defined as the ratio of the magnetic flux density  $\vec{B}$  measured at the center of the shield and the magnetic flux density without any shield at the same position.

There are two classes of magnetic shields at room temperature, viz., active and passive, which can be used either individually or in combination.

Passive magnetic shields are built from high-permeability materials with a high "conductivity" for magnetic fields. A shell of such material guides the external magnetic field around an inner volume, thus reducing the static magnetic field as well as the magnetic field variations in that volume.

The shielding effect of a passive shield of one layer is proportional to the layer thickness. For two separated layers, the shielding effect is the product of the shielding factors of the single shells if the distance in between is large enough.<sup>1,2</sup> Using multiple shield layers hence reduces the amount of expensive high-permeability material required to achieve the same shielding factor, but it increases the volume of the shield walls.

The field guiding effect of high-permeability materials is the dominating shielding effect only for magnetic disturbances with frequencies below about 1 Hz. For these frequencies, the shielding factor approaches a constant value, the quasi-static shielding factor, measured here with an excitation field oscillating at a frequency of  $f_{\text{ex}} = 0.01$  Hz. The rapid increase in shielding factor above 1 Hz is caused by the electrical conductivity of the shielding layer, and it can be further increased by an additional "eddy-current" layer. This is usually made of copper or copper-coated aluminum with a thickness of 5–12 mm.

For magnetic field disturbances above 1 kHz, the shielding factor is dominated by the radio-frequency (RF) shielding properties of the shield, which would be perfect for an electrically closed conducting surface, but in practice, it is limited by the size and design of the largest openings. If the openings are designed as electrically conducting pipes in the RF shield, the shielding effect can be maintained for larger frequencies if the length to diameter ratio is appropriately chosen. For most magnetic shields, the incorporated eddy-current shield is designed to simultaneously act as an RF shield.

A static active shield uses a constant current in an arrangement of coils to create a magnetic field that compensates for the surrounding field in the volume of interest. A dynamic active shield is a coil arrangement additionally equipped with one or more reference magnetic field sensors and a feedback control system that adjusts the current source driving the coils to compensate for the detected magnetic field variations, see, e.g., Refs. 3–6. The passive shield described

in this article will be finally surrounded by an active magnetic shielding installation to further enhance the shielding performance at frequencies below 5 Hz.

A common passive shielding material is permalloy, which is a nickel-iron alloy with nickel content above 75%. Various brand names with slightly different material compositions and properties exist. Their high permeability is achieved by a special annealing process in a reductive atmosphere at temperatures above  $\sim 1050$  °C. Another relevant manufacturing factor is the necessary careful handling of the material after annealing. Any mechanical stress acting on the material, for example, during bending, reduces its permeability. Large shields have to be assembled from flat sheets and edge pieces bent before annealing.

The first magnetic shields large enough for human use, used to measure the magnetic field of the heart or brain, were built in the 1960s.<sup>7–10</sup> Such large shields with two or more magnetic shielding layers and door access, called magnetically shielded rooms (MSRs), are nowadays commercially available from different companies.

Initially, the installation of large MSRs with more than two layers<sup>11–13</sup> was driven by the need for precise measurements of biomagnetic fields in the human body. For many years, the MSR with the highest shielding factor was "BMSR-2" at the Physikalisch-Technische Bundesanstalt, Berlin, Germany, with originally seven, now eight, magnetic shielding layers, having a shielding factor of 75 000<sup>14</sup> at 0.01 Hz, which was improved to 300 000 after a recent upgrade with an additional layer, which reduced the available shielded volume.<sup>15</sup>

Large multilayer shields were also pioneered in the field of fundamental physics measurements already in the 1980s, e.g., Refs. 16–20. One of the first large MSRs dedicated to physics experiments was built at the Oak Ridge National Laboratory,<sup>21</sup> followed by one at the Technical University of Munich.<sup>22,23</sup>

The MSR described in this work serves to shield the n2EDM apparatus, aimed at obtaining an improved measurement of the neutron electric dipole moment (nEDM).<sup>24</sup> The key requirement for n2EDM, besides a high shielding factor, is the ability to generate a very uniform magnetic field in the central 1 m<sup>3</sup> volume of the MSR.<sup>25</sup> The MSR design has to meet those requirements while complying with mechanical boundary conditions, such as shield geometry, size, weight, number and size of openings, and accessibility. The factors that affect the field uniformity are the magnetization state of the shielding metal, the homogeneity of a desired field produced by an internal coil system necessary for the nEDM experiment, and disturbances caused by the openings. Since these effects drop off with distance, MSRs with a large inner volume facilitate achieving good magnetic field uniformity, while MSRs with a smaller inner volume make it easier to achieve large shielding factors.<sup>2</sup> The design presented here is a compromise between these two factors, which optimizes the overall performance of our experiment. In this study, we demonstrate that the realized design achieves both a high shielding factor and a low and homogeneous enough magnetic field, which

results from low disturbances of field uniformity due to the MSR's magnetization state.

## II. DESIGN GUIDELINES

The MSR design was driven by the performance needed to reach the sensitivity goals of the n2EDM experiment and by the restrictions imposed by the apparatus to be installed inside the MSR.<sup>24</sup> Further constraints were set by the spatial dimensions of the installation area within the experimental hall.

The number and dimensions of the openings were determined by the components of the apparatus. Two very large openings with a diameter of 220 mm are required for the installation of the ultracold neutron guides. As a design principle, all openings are symmetrically mirrored on opposite MSR walls, which helps to suppress first-order gradients.

The doors must provide a minimum of  $2 \times 2 \text{ m}^2$  access for the inner chamber to allow for equipment installation, the largest one being the vacuum tank.

The key specified design performance criteria were (1) a quasi-static magnetic shielding factor at 0.01 Hz of 70 000 and (2) a remanent magnetic field in the central  $1 \text{ m}^3$  below 500 pT with a field gradient lower than 300 pT/m.

## III. CONSTRUCTION OF THE MSR

The MSR was engineered, designed, and constructed by VAC, Germany,<sup>26</sup> in an iterative process with input from the nEDM collaboration. The high-permeability materials used in all shielding layers were produced via smelting from the original ores in the furnaces of the VAC Hanau facility.

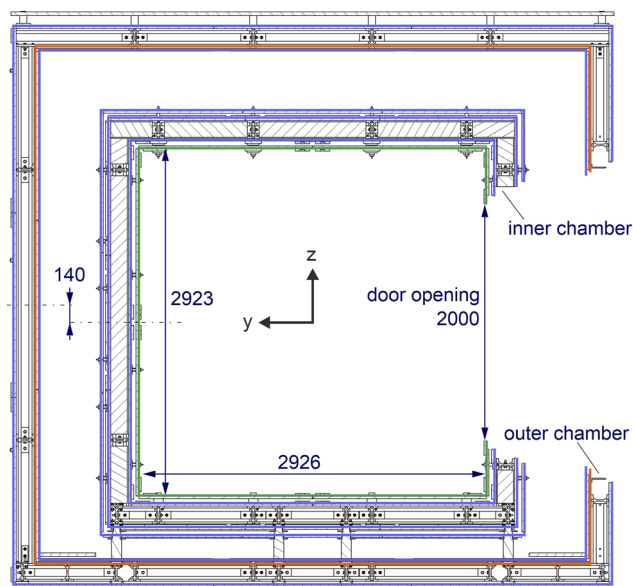


**FIG. 1.** Vertical cut showing the positioning and dimensions of the inner and outer chambers with shielding layers, with the MUMETALL<sup>®</sup> layers indicated in blue, ULTRAVAC<sup>®</sup> layer in green, and aluminum layer in red, as listed in Table I. All dimensions are in mm.

The MSR design consists of an outer and an inner chamber and an intermediate space as shown in Fig. 1. The inner chamber is centrally placed and separated from the outer chamber horizontally by a distance of  $\sim 45 \text{ cm}$  in all directions from the outer wall, with a vertical offset of 14 cm toward the floor. The intermediate space between the chambers shown in Fig. 2 is RF shielded, and it is magnetically shielded with a quasi-static shielding factor of about 65. It is accessible to workers and can be used for housing additional experimental equipment as well as sensitive signal electronics that are too magnetic to be located next to the central n2EDM apparatus. The outer dimensions of the MSR are  $5.2 \times 5.2 \text{ m}^2$  horizontally and 4.8 m vertically. The inner chamber is almost perfectly cubic with a side length of 2.92 m, thus featuring  $25 \text{ m}^3$  of internal volume for the installation of the experimental apparatus.

The presence of several openings in all six walls of the MSR provides access to and allows the operation of the n2EDM apparatus on the inside. The two neutron guides require the largest openings, with 220 mm diameter, with their centers separated by 550 mm. The diagram in Fig. 2 illustrates this arrangement. Identical openings on opposite sides of the chamber will be used for two pumping lines. Furthermore, nine large openings are symmetrically placed on the roof and the floor (Fig. 3), which will be used for, e.g., laser paths, optical fibers, cables, and sensor tubing. A few openings are present only either in the inner or in the outer chamber. The total number of openings amounts to 87, planned with contingency:

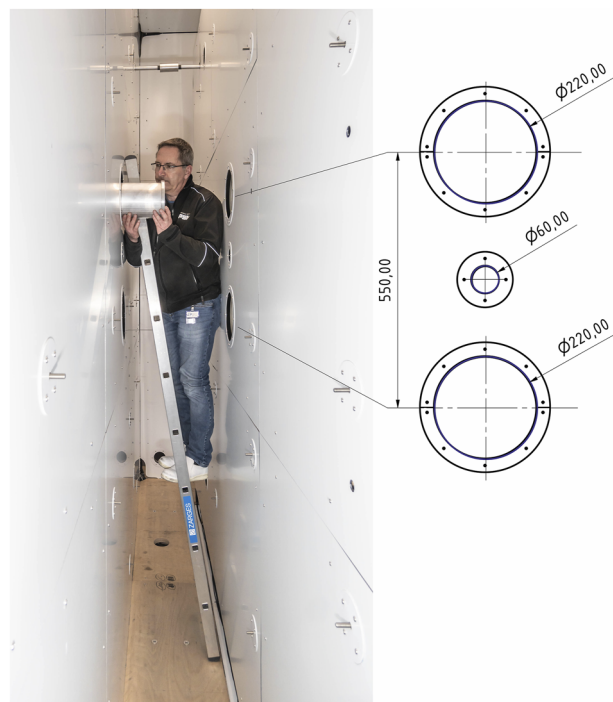


**FIG. 2.** Intermediate space between the inner and outer chamber. The image shows a test with a vacuum tube passing through one large opening. The diagram to the right depicts the dimensions and separation of the large openings in the center of the wall. All dimensions are in mm.

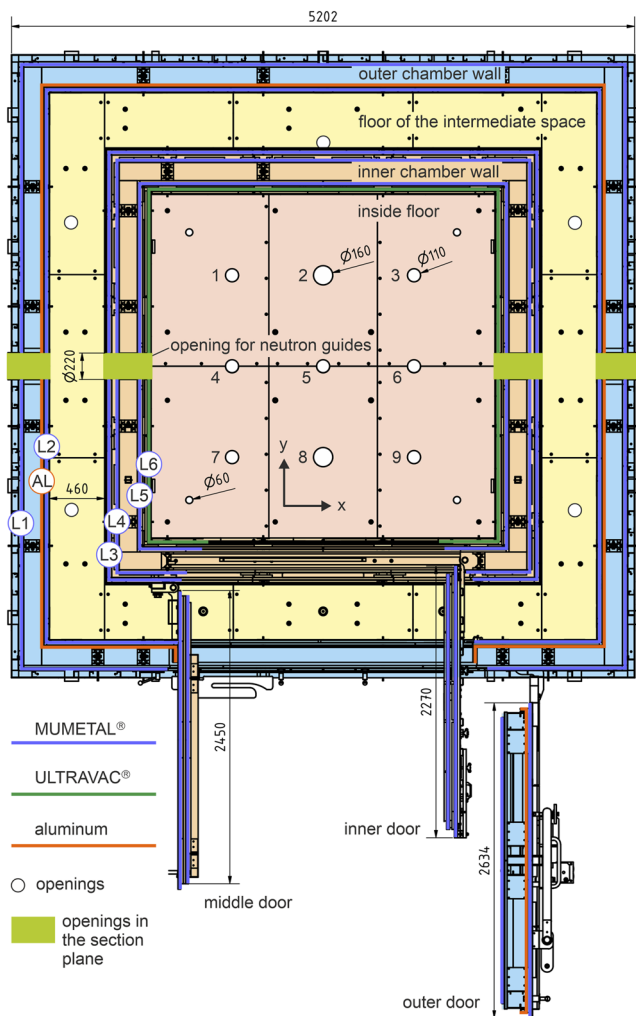


**FIG. 3.** Vertical section view onto the floor of the MSR. All dimensions are in mm. The layers are as given in Table I. There are two openings with an ID of 160 mm, seven openings with an ID of 110 mm, and four openings with an ID of 60 mm in the central region of the floor (roof). The pattern of openings in the floor is mirrored on the ceiling of the MSR. Some openings are numbered to allow the identification of measurement locations. Additional openings in the outside wall allow for external connections of the equipment that will be installed in the intermediate space.

- 4 with inner diameter (ID) = 220 mm,
- 4 with ID = 160 mm,
- 43 with ID = 110 mm (21 only in outer chamber),
- 2 with ID = 80 mm,
- 26 with ID = 60 mm (8 only in inner chamber), and
- 8 with ID = 55 mm.

Apart from the openings which are in one chamber only, all openings are coaxially passing through the inner and outer chamber walls. Figure 3 provides a sense of the arrangement of the openings in the floor of the MSR.

The assembled MSR, installed in the experimental area south of the ultracold neutron (UCN) source<sup>27,28</sup> at the Paul Scherrer

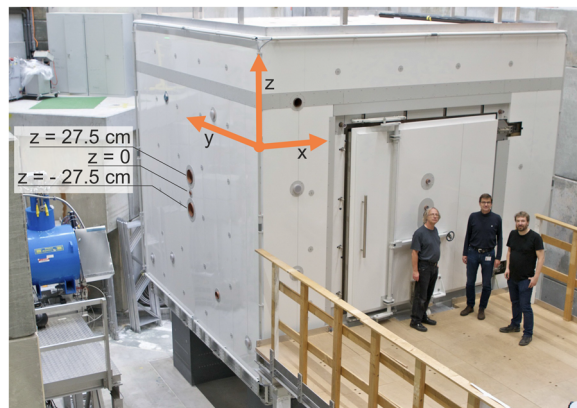


**FIG. 4.** The MSR installed in the area south of the PSI UCN source. The experiment's coordinate system is indicated. The openings used for the horizontal scans along the x axis (see Fig. 13) are labeled with their z-coordinates.

Institute (PSI), is shown in Fig. 4 from the side of the entrance door and in Fig. 5 from the rear. It is placed on an aluminum frame positioned on four 1364 mm high granite pillars with a  $1 \times 1 \text{ m}^2$  base, all placed on top of its own concrete foundation, vibrationally isolated from the surrounding concrete floor of the experimental hall.

The MSR consists of seven shielding layers (Table I), with one aluminum layer acting as eddy-current and RF shield. Of the six soft magnetic layers, the five outer ones are made of MUMETALL (Ni 77%, Cu 4.5%, Mo 3.3%, Fe balance), a soft magnetic NiFe alloy with a Z-shaped hysteresis curve<sup>29</sup> and correspondingly high maximum permeability. MUMETALL is a standard alloy used for magnetic shielding. However, the alloy ULTRAVAC 816 (Ni 81%, Mo 6%, Fe balance) employed for the innermost layer was applied here for the first time in MSRs. This novel NiFe alloy has a round-loop-shaped hysteresis curve due to its composition.<sup>29</sup> In



**FIG. 5.** View of the rear side of the MSR. Two of the tubes carrying the excitation coils used to measure the shielding factor are indicated. The openings used for the horizontal scans along the y axis (see Fig. 14) are labeled with their z-coordinates.

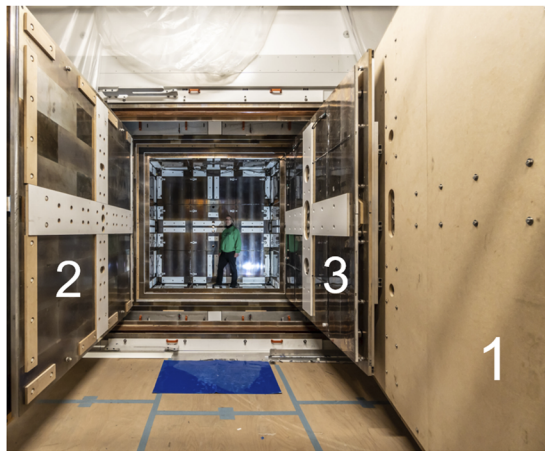
**TABLE I.** Naming scheme and thicknesses of all shielding layers.

Chamber	Layer	Thickness (mm)	Material
Outer	L1	3.75	MUMETALL
Outer	Al	8.00	Aluminum
Outer	L2	3.75	MUMETALL
Inner	L3	6.75	MUMETALL
Inner	L4	6.75	MUMETALL
Inner	L5	4.5	MUMETALL
Inner	L6	6.0	ULTRAVAC

this alloy, remagnetization processes take place mainly via reversible domain wall motion. This material is characterized by high initial permeability even at saturation levels of magnetic field strength  $H < 0.1$  A/m in the shielding layer and by a lower maximum permeability compared to MUMETALL. Due to its round-loop-shaped hysteresis curve, the remanence of ULTRAVAC 816 with a residual magnetic flux density  $B_r = 0.2\text{--}0.3$  T is less than half that of MUMETALL ( $B_r = 0.45\text{--}0.55$  T). This hysteresis shape allows for an optimal demagnetization of the innermost layer to achieve minimum residual fields. All the walls were manufactured using the VAC proprietary panel technique.

All the additional materials used in the MSR construction were previously checked for magnetic contamination with different specifications. The most stringent restrictions applied to materials in the inner chamber, allowing for a maximum 200 pT signal at 50 mm distance, when scanned in the BMSR-2 magnetic testing facility at PTB, Berlin.<sup>14</sup> Expanded polystyrene placed between the individual layers served as thermal insulation.

Figure 6 shows a photograph of the open MSR with the doors visible on the sides. Information about the dimensions can be found in Fig. 3. All doors are larger than the door openings. The overlap is necessary to reduce the magnetic resistance for the field when passing from the wall to the door. On all the doors, dedicated aluminum plates allow the mechanical contact pressure to be increased. The opening and closing operations are fully manual and can be done in


**FIG. 6.** View of the MSR with all three numbered doors open.

about 20 min. With a weight of 1500 kg, the outermost door needs to be supported by an additional wheel.

#### IV. SHIELDING FACTOR

The shielding factor was measured using excitation coils on the outer edges of all the outermost walls of the MSR (see Fig. 5). The coil constants  $K_{ex}$  of those coils were calibrated with an additional external coil system, which had been mounted on a large frame before the installation of the MSR. The distance of these coils to the later position of the MSR walls was  $\sim 1.5$  m. The excitation coils produced a sinusoidal signal  $B_{ex} = K_{ex} I_{ex} \sin(2\pi f_{ex} t)$  with  $2 \mu\text{T}$  peak-to-peak amplitude at the MSR center position. A QuSpin<sup>®</sup> magnetometer<sup>30</sup> recorded the excitation signal inside the inner chamber. The sensor was installed in the center of the chamber, inside a small calibration coil that generated a sinusoidal reference signal  $B_{ref} = K_{ref} I_{ref} \sin(2\pi f_{ref} t)$  with the reference frequency  $f_{ref}$  well separated from the excitation frequency  $f_{ex}$ . The coil constant  $K_{ref}$  of the reference coil was independently measured and was found to agree to better than 1% with the calculated value. During data collection, the magnetometer signal and the monitor signals for the two currents in the coils  $I_{ex}$  and  $I_{ref}$  were recorded by a multichannel analog-to-digital converter (ADC) synchronized with the function generator that supplied the  $f_{ex}$  and  $f_{ref}$  signals. The duration of the time series recorded by the ADC for each test frequency was programmed such that it contained an exact integer multiple of the oscillation periods of  $f_{ex}$  and  $f_{ref}$ . This simplified the data analysis since each oscillation signal was guaranteed to contribute only to a single frequency bin in the Fast Fourier Transformation (FFT) spectrum of the time series. This method minimizes the influence of external disturbances on the final result because any noise in frequency bins other than the ones centered at  $f_{ex}$  and  $f_{ref}$  is disregarded. The applied FFT algorithm extracted the root-mean-square amplitudes of the signals at the relevant frequencies. Those were the amplitude of the current in the excitation coil  $I_{ex}^{rms}$ , the amplitude of the current in the reference coil  $I_{ref}^{rms}$ , the magnetometer signal at the excitation frequency  $B_{ex}^{rms}$ , and the magnetometer signal at the reference frequency  $B_{ref}^{rms}$ . Comparing the measured reference signal to the expected amplitude gave us an in-place correction factor  $C_{cal}$  for the calibration of the magnetometer,

$$C_{cal} = \frac{B_{ref}^{rms}}{K_{ref} I_{ref}^{rms}}. \quad (1)$$

The shielding factor  $F_S$  is obtained in a similar way by comparing the measured amplitude at the excitation frequency to the value calculated from the coil constant and current,

$$F_S = \frac{K_{ex} I_{ex}^{rms}}{B_{ex}^{rms}} C_{cal} = \frac{K_{ex} I_{ex}^{rms}}{B_{ex}^{rms}} \frac{B_{ref}^{rms}}{K_{ref} I_{ref}^{rms}}. \quad (2)$$

The measurement method results are independent of the magnetometer calibration and dependent only on amplitude measurements and coil constants, which were independently cross-checked. The measurement was performed for the three spatial directions in almost the same way. Only the density of excitation frequencies  $f_{ex}$  was increased for the  $x$  and  $z$  directions in order to investigate the noise above 5 Hz.

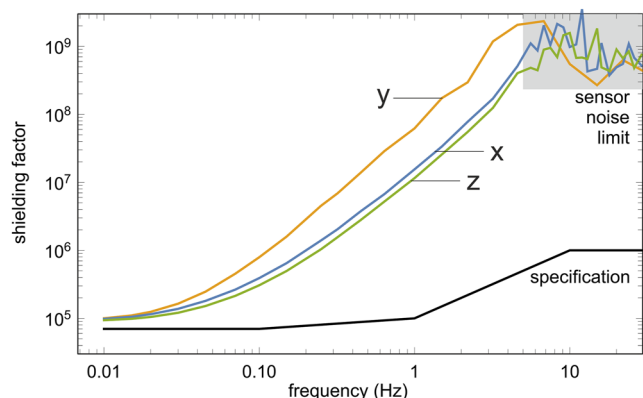


**FIG. 7.** Dependence of the magnetic shielding factor on frequency measured with a sinusoidal  $2 \mu\text{T}$  peak-to-peak signal for the three spatial dimensions as defined in Fig. 4. The black line shows the specified minimum required shielding factor for the depicted frequency range. The gray shaded area shows the region where the excitation signal is reduced to the level of the sensor noise due to the shield.

The measured frequency-dependent shielding factor is shown in Fig. 7. At frequencies above 5 Hz, the shielding factor is so large that the sensor reaches its noise limit. Additionally, the measurement above 5 Hz shows interference from the PSI magnetic environment, which leads to fluctuating results, with a minimum shielding factor of  $10^8$ . The specified performance is surpassed at all the measured frequencies.

The quasi-static shielding factor at 0.01 Hz, which is the most important for the n2EDM experiment, is  $\sim 100\,000$  in all the spatial directions:  $101\,300 \pm 500$  in the  $x$  direction,  $101\,000 \pm 1000$  in the  $y$  direction, and  $94\,900 \pm 1400$  in the  $z$  direction.

Figure 7 also shows that for frequencies between 0.03 and 5 Hz, the shielding factor in the  $y$  direction is consistently larger than in the other directions. This behavior is expected since the eddy current induced by a magnetic disturbance in the  $y$  direction is not crossing the door contacts, which are, in terms of electric conductivity, the weakest link in the eddy-current shield. A comparison of the performance in the  $x$  and  $y$  directions thus gives an estimate of the losses caused by the imperfect magnetic and electric contacts of the doors.

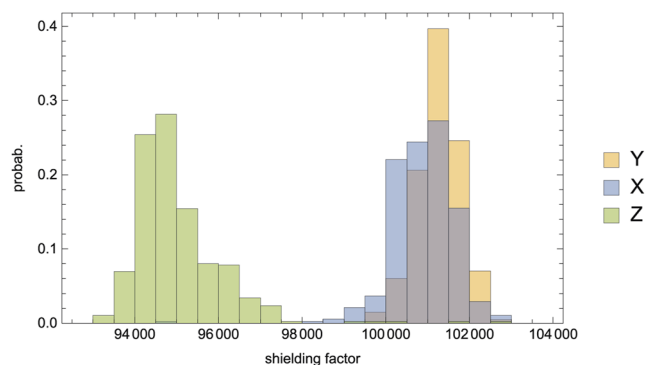


**FIG. 8.** Histogram of all the measurements of the quasi-static shielding factor at 0.01 Hz in the three spatial directions.

A histogram of the individual shielding factor measurements at 0.01 Hz is shown in Fig. 8. The quasi-static shielding factor in the  $z$  direction is slightly smaller than in the other directions. This is caused by the smaller distance and the offset between the inner and outer chambers in the vertical direction. The spread is likely due to a combination of the statistical uncertainty of the measurement and the changing magnetic environments over the course of the measurements, which also causes a small change in the shield response.

## V. EQUILIBRATION OF MSR LAYERS

In order to minimize the remanent field in the inner chamber, all MSR walls need to be demagnetized,<sup>31</sup> or more precisely “equilibrated,”<sup>32</sup> to achieve the most energetically favorable state. This process is also sometimes colloquially referred to as “degaussing.” Therefore, four coils per spatial direction are installed with cables along the edges of every wall of layers 1–6 individually, as sketched in Fig. 9, similar to what is shown in Fig. 2 of Ref. 32, thus allowing the driving of a magnetic flux independently in the three spatial dimensions. Such an arrangement was first used in Ref. 32 for the “ZUSE” chamber at PTB, Berlin, and was also used in Ref. 33. Here, layer 6 has additional coils distributed over the width of the walls and the door to further improve the equilibration procedure for the innermost layer.<sup>34</sup>

A reproducible and good equilibration result is obtained with a sequential equilibration procedure driving an oscillating magnetic

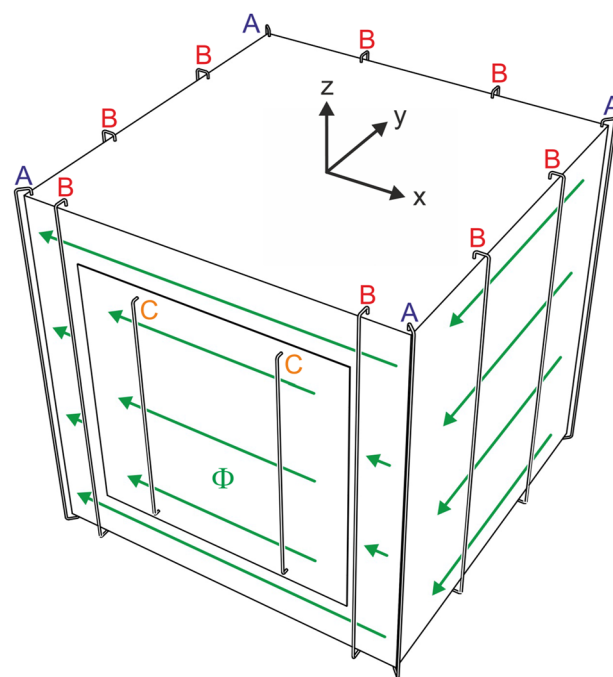


**FIG. 9.** Arrangement of the equilibration coils in the  $z$  direction on one MSR layer drawn as a cube box. Label A: corner coils on all layers; label B: additional coils only on layer 6; label C: additional smaller coils only on the layer 6 door. The green arrows indicate the direction of the magnetic flux  $\Phi$  produced by a current through the indicated coils.

flux, with the amplitude first increasing, then being slowly ramped down to zero. All six layers are subsequently equilibrated starting at the outermost layer. In the initial characterization measurements, a 5 Hz sinusoidal signal was used to drive the current. A standard equilibration procedure took about 5 h and was repeated after every opening of the MSR doors. A more detailed description of the final optimized equilibration procedure will be part of a forthcoming publication.

## VI. REMANENT MAGNETIC FIELD

### A. Measurement procedure

For this investigation, the magnetic field in the inner chamber was measured with a low-noise Bartington MAG03 three-axis fluxgate<sup>35</sup> located in a plexiglass tube installed between opposite openings in the MSR walls. Position scans were recorded by sliding the fluxgate along the axes of this tube using a pushrod. The rod has pin holes every 100 mm that were used to reproducibly fix the position along the tube as well as the rotation of the fluxgate around the axis of the tube. The front view of this setup is depicted in Fig. 10. The accessible measurement positions range from  $-60$  to  $+140$  cm relative to the center of the chamber. At  $140$  cm, the fluxgate sensors are as close as  $7$  cm to the ULTRAVAC surface of the innermost shielding layer.

A typical measurement consisted of integrating the sensor signals for  $3$  s and then rotating the fluxgate by  $90^\circ$ . This procedure was repeated until all four orientations ( $0^\circ, 90^\circ, 180^\circ, 270^\circ$ ) of the fluxgate were recorded before proceeding to the next position along the tube. The rotation allowed the compensation of the sensor offsets in the two transverse directions since the contribution of the local magnetic field to the sensor reading must invert when the sensors are rotated by  $180^\circ$ .

When scanning in the vertical direction, the tube could be installed from the outside so that the MSR doors did not have to be opened between measurements and the equilibration procedure did not have to be repeated. This means the magnetic configuration

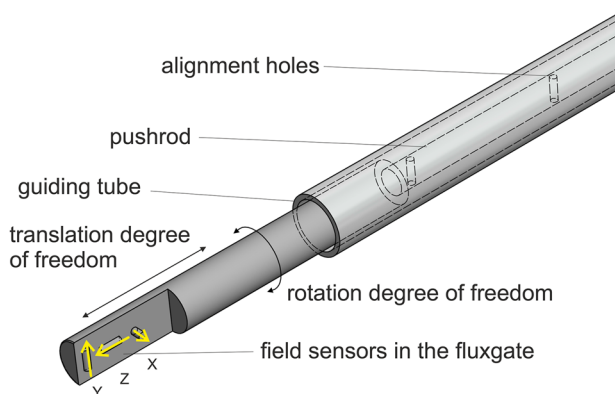


**FIG. 10.** Scheme of the fluxgate sensor in the guiding tube. The rotation degree of freedom is used to determine the DC-offset for absolute field measurements for the transverse sensors ( $x$  and  $y$ ). A pin through the holes in the pushrod was used to fix both the rotation and translation. The directions of the  $x$ ,  $y$ , and  $z$  component sensors are indicated by arrows.

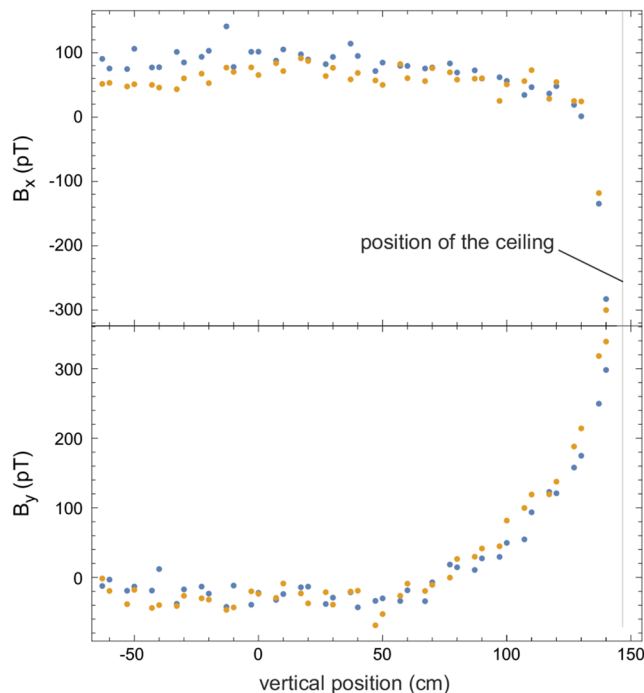


**FIG. 11.** Results from two vertical scans of the remanent magnetic field inside the MSR along the same axis. The recordings were taken four days apart, with the blue dots indicating the first measurement. The magnetic configuration of the MSR was not changed during this time.

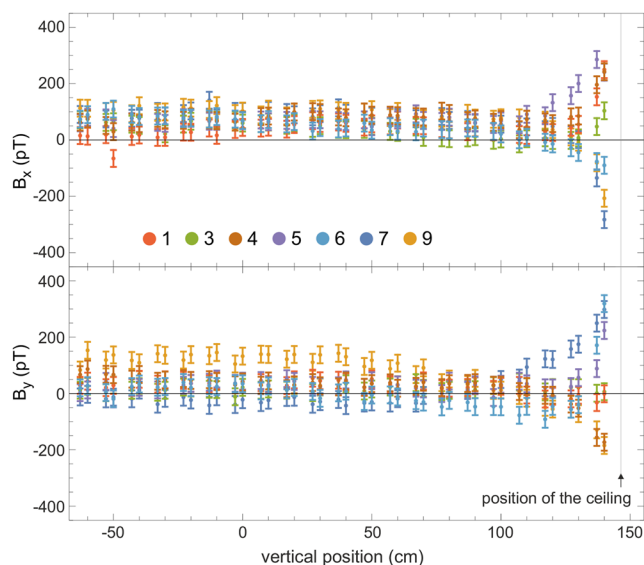


**FIG. 12.** All  $B_x$  and  $B_y$  field values measured in the different vertical scans. The remanent field increases to values of about  $300$  pT, only when approaching the ULTRAVAC wall of the inner chamber. Each color represents a vertical  $B_x$  and  $B_y$  scan through one of the openings in the roof. The numbers next to the colored filled circles reference the position of the openings as depicted in Fig. 3.



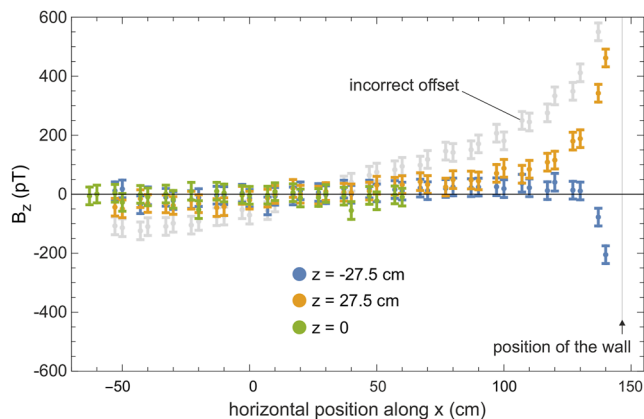


**FIG. 13.**  $B_z$  field values measured in a horizontal scan along  $x$  at the position of the three large openings shown in the diagram of Fig. 2, at the center of the MSR ( $z = 0$ ) and above (27.5 cm) and below (−27.5 cm) the center. The remanent field increases to values of about 500 pT only when approaching the ULTRAVAC wall of the inner chamber. One measurement series depicted by the gray dots displays significantly larger remanent field values. This was later found to be due to an equilibration procedure with an incorrect offset. The gray color shows the measurement with incorrect offset of the equilibration procedure. The gray line indicates the position of the wall, i.e., layer 6.

of the MSR was unchanged except for possible relaxation processes in the wall material. All other measurements were performed after an equilibration of all shield layers.

## B. Results

In order to assess the repeatability of the magnetic field measurements, we repeated one vertical scan after four days. Figure 11 compares the offset-corrected measurements from both these scans. The root mean square of the differences between the two measurements is 21 and 24 pT for the  $x$  and  $y$  directions, respectively. The total deviation is close to the expected statistical uncertainty but also shows a small systematic component, especially in  $B_x$ , where the

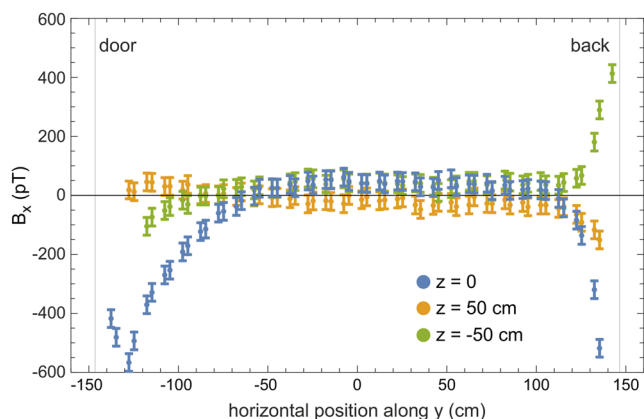


**FIG. 14.**  $B_x$  field values measured in a scan along the  $y$  axis at the position of three openings in the door at the center ( $z = 0$ ) and above (50 cm) and below (−50 cm) the center. The gray lines indicate the position of the door and the back wall.

mean difference between all points of the scans amounts to 18 pT. Combining these two deviations, we conservatively estimate the total measurement error to be 30 pT, which is reflected by the error bars shown in Figs. 12–14.

All measured values for  $B_x$  and  $B_y$  taken during vertical scans in different positions are shown in Fig. 12, which shows the results obtained after a single equilibration procedure. Figure 13 shows the  $B_z$  field component, which was measured in a horizontal scan after equilibration performed on different days since the doors had to be opened in order to install the tube for the fluxgate.

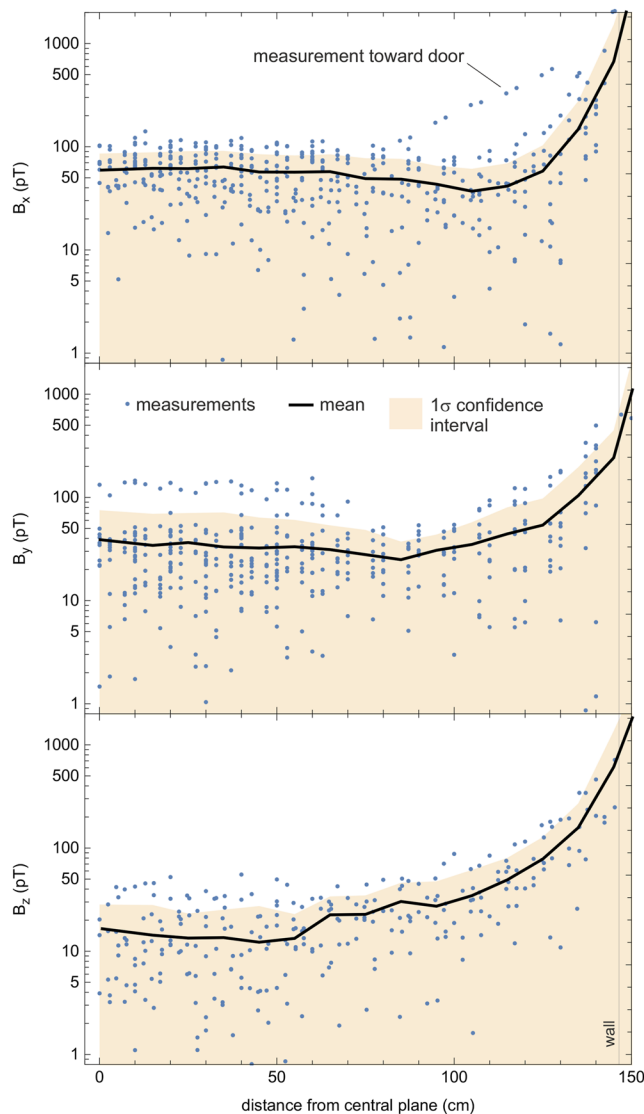


**FIG. 15.** Summary of all measured scans of the three field components  $B_x$ ,  $B_y$ , and  $B_z$  performed after equilibration of the MSR. The magnitude of the magnetic field components is shown as a function of distance to a central plane perpendicular to the scan direction. All points in the central cubic meter thus fall into the region with distance smaller than 50 cm. The black lines give the mean values with the  $1\sigma$  uncertainties displayed as the shaded area.

The largest deviation from ideal behavior was found in a horizontal scan along the  $y$  direction. The corresponding measurements of  $B_x$  are shown in Fig. 14. Here, the mechanical scan range was increased to reach from wall to wall. The measurements show the expected effect that repeating an equilibration leads to the strongest magnetic field uncertainties close to the wall and especially close to the door.

Already with a non-optimized equilibration procedure, we find a large volume, ranging from  $-76$  to  $76$  cm in  $x$  and  $y$ , and  $-60$  to  $140$  cm in  $z$ , in which all the measured field values for  $B_x$ ,  $B_y$ , and  $B_z$  are below  $150$  pT, originally specified to be below  $500$  pT. Positions at lower  $x$ ,  $y$ , and  $z$  values could not be measured with the described setup. The gradients in the central  $1\text{ m}^3$  were significantly smaller than originally specified ( $300$  pT/m, see Sec. II). In this volume, the gradients are within the statistical uncertainty of the fluxgate sensors used, which is estimated to correspond to  $60$  pT/m at  $1\sigma$  confidence level.

The remanent magnetic field measurements along the three spatial directions are summarized in Fig. 15 relative to their distance from the center of the inner chamber. This distance is computed relative to a plane through the center and perpendicular to the scan direction. Hence, all the measured points in the central  $1\text{ m}^3$  volume are at a distance  $<50$  cm. The ULTRAVAC material of the layer 6 wall is at a distance of  $146.5$  cm. One can see that all  $1\sigma$  confidence intervals in the central  $8\text{ m}^3$  (positions  $<100$  cm) are below  $100$  pT. For the  $z$  component of the magnetic field also, which is the most important for n2EDM, the maximum deviation is below  $100$  pT in the central  $8\text{ m}^3$ . Only when approaching the wall, the remanent field values slowly increase to  $\sim 500$  pT at a distance of about  $4$  cm from the ULTRAVAC.

## VII. SUMMARY

We constructed a unique magnetically shielded room with excellent performance, providing  $25\text{ m}^3$  of usable shielded volume for the n2EDM apparatus, which will search for the neutron electric dipole moment with a baseline sensitivity of  $10^{-27}e$  cm. This MSR provides the largest ultralow magnetic field environment in the world despite its numerous openings allowing for access and throughgoing connections.

Such a magnetic performance is achieved using five MUMET-ALL layers, one ULTRAVAC layer, and one aluminum layer. A quasi-static shielding factor at  $0.01$  Hz of  $\sim 100\,000$  was measured in all three spatial directions. The shielding factor rapidly increases with frequency and already reaches  $10^8$  for frequencies above  $3$  Hz.

After applying the equilibration procedure, the MSR was found to provide an exceptionally low magnetic field environment across a large volume. As the other magnetic field components, in particular the most important field component  $B_z$  (vertical) shows remanent magnetic field values below  $100$  pT in the central  $8\text{ m}^3$ .

## ACKNOWLEDGMENTS

We acknowledge the dedicated work of Lela Bauer, Markus Hein, and Michael Wüst, comprising the group for magnetically shielded rooms in the company VAC-Vacuumschmelze, Hanau; the support of Michael Meier in the planning and construction stages;

support of Thomas Stapf in the design and installation stages; and the technical support provided by Luke Noorda. We appreciate the help provided by the PSI support groups in the installation stage. Financial support by the Swiss National Science Foundation R'EQUIP under Grant No. 139140, by PSI, and by the Emil-Berthel-Fonds is acknowledged. The material scans inside BMSR-2 were supported by the Core Facility "Metrology of Ultra-Low Magnetic Fields" at Physikalisch-Technische Bundesanstalt, which received funding from the Deutsche Forschungsgemeinschaft-DFG (funding codes: Grant Nos. DFG KO 5321/3-1 and TR 408/11-1). Support by the Swiss National Science Foundation Project Nos. 200020-188700 (PSI), 200020-163413 (PSI), 200011-178951 (PSI), 172626 (PSI), 169596 (PSI), 200021-181996 (Bern), 200441 (ETH), FLARE 20FL21-186179, and 20FL20-201473 is gratefully acknowledged. The LPC Caen and the LPSC Grenoble acknowledge the support of the French Agence Nationale de la Recherche (ANR) under Reference No. ANR-14-CE33-0007 and the ERC Project No. 716651-NEDM. University of Bern acknowledges the support received via the European Research Council under the ERC Grant Agreement No. 715031-Beam-EDM. The Polish collaborators wish to acknowledge support from the National Science Center, Poland, under Grant Nos. 2018/30/M/ST2/00319 and 2020/37/B/ST2/02349. Support by the Cluster of Excellence "Precision Physics, Fundamental Interactions, and Structure of Matter" (Grant No. PRISMA+EXC 2118/1) funded by the German Research Foundation (DFG) within the German Excellence Strategy (Project No. 39083149) is acknowledged. Collaborators at the University of Sussex wish to acknowledge support from the School of Mathematical and Physical Sciences, as well as from the STFC under Grant No. ST/S000798/1. This work was partly supported by the Fund for Scientific Research Flanders (FWO), and Project No. GOA/2010/10 of the KU Leuven. Researchers from the University of Belgrade acknowledge institutional funding provided by the Institute of Physics Belgrade through a grant by the Ministry of Education, Science and Technological Development of the Republic of Serbia.

## AUTHOR DECLARATIONS

### Conflict of Interest

The authors have no conflicts to disclose.

### Author Contributions

**N. J. Ayres:** Writing – review & editing (equal). **G. Ban:** Writing – review & editing (equal). **G. Bison:** Writing – review & editing (equal). **K. Bodek:** Writing – review & editing (equal). **V. Bondar:** Writing – review & editing (equal). **T. Bouillaud:** Writing – review & editing (equal). **B. Clement:** Writing – review & editing (equal). **E. Chanel:** Writing – review & editing (equal). **P.-J. Chiu:** Writing – review & editing (equal). **C. B. Crawford:** Writing – review & editing (equal). **M. Daum:** Writing – review & editing (equal). **C. B. Doorenbos:** Writing – review & editing (equal). **S. Emmenegger:** Writing – review & editing (equal). **A. Fratangelo:** Writing – review & editing (equal). **M. Fertl:** Writing – review & editing (equal). **W. C. Griffith:** Writing – review & editing (equal). **Z. D. Grujic:** Writing – review & editing (equal). **P. G. Harris:** Writing – review & editing (equal). **K. Kirch:** Writing – review & editing (equal). **J. Krempel:**

Writing – review & editing (equal). **B. Lauss:** Writing – review & editing (equal). **T. Lefort:** Writing – review & editing (equal). **O. Naviliat-Cuncic:** Writing – review & editing (equal). **D. Pais:** Writing – review & editing (equal). **F. M. Piegsa:** Writing – review & editing (equal). **G. Pignol:** Writing – review & editing (equal). **G. Rauscher:** Writing – review & editing (equal). **D. Rebreyend:** Writing – review & editing (equal). **I. Rienäcker:** Writing – review & editing (equal). **D. Ries:** Writing – review & editing (equal). **S. Roccia:** Writing – review & editing (equal). **D. Rozpedzik:** Writing – review & editing (equal). **W. Saenz-Arevalo:** Writing – review & editing (equal). **P. Schmidt-Wellenburg:** Writing – review & editing (equal). **A. Schnabel:** Writing – review & editing (equal). **N. Severijns:** Writing – review & editing (equal). **M. Staab:** Writing – review & editing (equal). **K. Svirina:** Writing – review & editing (equal). **R. Tavakoli Dinani:** Writing – review & editing (equal). **J. Thorne:** Writing – review & editing (equal). **N. Yazdandoost:** Writing – review & editing (equal). **J. Zejma:** Writing – review & editing (equal). **G. Zsigmond:** Writing – review & editing (equal).

## DATA AVAILABILITY

The data that support the findings of this study are available on request from the corresponding authors. The datasets generated and/or analyzed during the current study are not publicly available.

## REFERENCES

- 1 D. Dubbers, “Simple formula for multiple mu-metal shields,” *Nucl. Instrum. Methods Phys. Res., Sect. A* **243**, 511–517 (1986).
- 2 R. Boll, *Weichmagnetische Werkstoffe: Einfuehrung in den Magnetismus. VAC Werkstoffe und ihre Anwendungen*, 4th ed. (Vacuumschmelze GmbH, 1990).
- 3 R. L. Driscoll and P. T. Olsen, “Compensation of Earth’s field variations by field controlled rubidium oscillator,” *Rev. Sci. Instrum.* **42**, 1427–1431 (1971).
- 4 H. J. M. ter Brake, H. J. Wieringa, and H. Rogalla, “Improvement of the performance of a mu-metal magnetically shielded room by means of active compensation (biomagnetic applications),” *Meas. Sci. Technol.* **2**, 596–601 (1991).
- 5 S. Afach *et al.*, “Dynamic stabilization of the magnetic field surrounding the neutron electric dipole moment spectrometer at the Paul Scherrer Institute,” *J. Appl. Phys.* **116**, 084510 (2014).
- 6 M. Rawlik, A. Eggenberger, J. Krempel, C. Crawford, K. Kirch, F. M. Piegsa, and G. Quémener, “A simple method of coil design,” *Am. J. Phys.* **86**, 602–608 (2018).
- 7 D. Cohen, “Enhancement of ferromagnetic shielding against low-frequency magnetic fields,” *Appl. Phys. Lett.* **10**, 67–69 (1967).
- 8 D. Cohen, “Magnetic fields around the torso: Production by electrical activity of the human heart,” *Science* **156**, 652–654 (1967).
- 9 D. Cohen, “Magnetoencephalography: Evidence of magnetic fields produced by alpha-rhythm currents,” *Science* **161**, 784–786 (1968).
- 10 D. Cohen, E. A. Edelsack, and J. E. Zimmerman, “Magnetocardiograms taken inside a shielded room with a superconducting point-contact magnetometer,” *Appl. Phys. Lett.* **16**, 278–280 (1970).
- 11 A. Mager, “The Berlin magnetically shielded room (BMSR), section A: Design and construction,” in *Proceedings of the Third International Workshop* (De Gruyter, Berlin, 1981), pp. 51–78.
- 12 V. Kelha, J. Pukki, R. Peltonen, A. Penttinen, R. Ilmonemi, and J. Heino, “Design, construction, and performance of a large-volume magnetic shield,” *IEEE Trans. Magn.* **18**, 260–270 (1982).
- 13 G. Kajiwara, K. Harakawa, H. Ogata, and H. Kado, “High-performance magnetically shielded room,” *IEEE Trans. Magn.* **32**, 2582–2585 (1996).
- 14 J. Bork, H. Hahlbohm, R. Klein, and A. Schnabel, “The 8-layered magnetically shielded room of the PTB,” in *Biomag 2000: Proceedings of the 12th International Conference on Biomagnetism* (2000), pp. 970–973.
- 15 T. Liu, A. Schnabel, J. Voigt, W. Kilian, Z. Sun, L. Li, and L. Trahms, “A built-in coil system attached to the inside walls of a magnetically shielded room for generating an ultra-high magnetic field homogeneity,” *Rev. Sci. Instrum.* **92**, 024709 (2021).
- 16 C. E. Loving and P. G. H. Sandars, “On the feasibility of an atomic-beam resonance experiment sensitive to the nuclear-spin-dependent weak neutral current interaction,” *J. Phys. B: At. Mol. Phys.* **10**, 2755–2766 (1977).
- 17 I. S. Altarev, Y. V. Borisov, N. V. Borovikova, A. B. Brandin, A. I. Egorov, V. F. Ezhov, S. N. Ivanov, V. M. Lobashev, V. A. Nazarenko, V. L. Ryabov, A. P. Serebrov, and R. R. Taldaev, “A new upper limit on the electric dipole moment of the neutron,” *Phys. Lett. B* **102**, 13–16 (1981).
- 18 J. M. Pendlebury, K. F. Smith, R. Golub, J. Byrne, T. J. L. McComb, T. J. Sumner, S. M. Burnett, A. R. Taylor, B. Heckel, N. F. Ramsey, K. Green, J. Morse, A. I. Kilvington, C. A. Baker, S. A. Clark, W. Mampe, P. Ageron, and P. C. Miranda, “Search for a neutron electric dipole moment,” *Phys. Lett. B* **136**, 327–330 (1984).
- 19 S. K. Lamoreaux, J. P. Jacobs, B. R. Heckel, F. J. Raab, and N. Fortson, “New constraints on time-reversal asymmetry from a search for a permanent electric dipole moment of Hg199,” *Phys. Rev. Lett.* **59**, 2275–2278 (1987).
- 20 K. F. Smith, N. Crampin, J. M. Pendlebury, D. J. Richardson, D. Shiers, K. Green, A. I. Kilvington, J. Moir, H. B. Prosper, D. Thompson, N. F. Ramsey, B. R. Heckel, S. K. Lamoreaux, P. Ageron, W. Mampe, and A. Steyerl, “A search for the electric dipole moment of the neutron,” *Phys. Lett. B* **234**, 191–196 (1990).
- 21 H. Soltner, U. Pabst, M. Butzek, M. Ohl, T. Kozielski, M. Monkenbusch, D. Sokol, L. Maltin, E. Lindgren, S. Koch, and D. Fugate, “Design, construction, and performance of a magnetically shielded room for a neutron spin echo spectrometer,” *Nucl. Instrum. Methods Phys. Res., Sect. A* **644**, 40–47 (2011).
- 22 I. Altarev, E. Babcock, D. Beck, M. Burghoff, S. Chesnevskaya, T. Chupp, S. Degenkolb, I. Fan, P. Fierlinger, A. Frei, E. Gutschiedl, S. Knappe-Grüneberg, F. Kuchler, T. Lauer, P. Link, T. Lins, M. Marino, J. McAndrew, B. Niessen, S. Paul, G. Petzoldt, U. Schlöpfer, A. Schnabel, S. Sharma, J. Singh, R. Stoepler, S. Stuiber, M. Sturm, B. Taubenheim, L. Trahms, J. Voigt, and T. Zechlau, “A magnetically shielded room with ultra low residual field and gradient,” *Rev. Sci. Instrum.* **85**, 075106 (2014); [arXiv:1403.6467](https://arxiv.org/abs/1403.6467) [physics.ins-det].
- 23 I. Altarev, M. Bales, D. H. Beck, T. Chupp, K. Fierlinger, P. Fierlinger, F. Kuchler, T. Lins, M. G. Marino, B. Niessen, G. Petzoldt, U. Schlöpfer, A. Schnabel, J. T. Singh, R. Stoepler, S. Stuiber, M. Sturm, B. Taubenheim, and J. Voigt, “A large-scale magnetic shield with 106 damping at millihertz frequencies,” *J. Appl. Phys.* **117**, 183903 (2015).
- 24 N. J. Ayres *et al.*, “The design of the n2EDM experiment,” *Eur. Phys. J. C* **81**, 512 (2021).
- 25 C. Abel, N. J. Ayres, T. Baker, G. Ban, G. Bison, K. Bodek, V. Bondar, C. B. Crawford, P.-J. Chiu, E. Chanel, Z. Chowdhuri, M. Daum, B. Dechenaux, S. Emmenegger, L. Ferraris-Bouchez, P. Flaux, P. Geltenbort, K. Green, W. C. Griffith, M. van der Grinten, P. G. Harris, R. Henneck, N. Hild, P. Iaydjiev, S. N. Ivanov, M. Kasprzak, Y. Kermaidic, K. Kirch, H.-C. Koch, S. Komposch, P. A. Koss, A. Kozela, J. Krempel, B. Lauss, T. Lefort, Y. Lemièrre, A. Leredde, P. Mohanmurthy, D. Pais, F. M. Piegsa, G. Pignol, G. Quemener, M. Rawlik, D. Rebreyend, D. Ries, S. Roccia, D. Rozpedzik, P. Schmidt-Wellenburg, A. Schnabel, N. Severijns, R. Viro, A. Weis, E. Wursten, G. Wyszynski, J. Zejma, and G. Zsigmond, “Magnetic-field uniformity in neutron electric-dipole-moment experiments,” *Phys. Rev. A* **99**, 042112 (2019).
- 26 VACUUMSCHMELZE GmbH & Co. KG, Gruener Weg 37, D-63450 Hanau, Germany.
- 27 G. Bison, B. Blau, M. Daum, L. Göttl, R. Henneck, K. Kirch, B. Lauss, D. Ries, P. Schmidt-Wellenburg, and G. Zsigmond, “Neutron optics of the PSI ultracold-neutron source: Characterization and simulation,” *Eur. Phys. J. A* **56**, 33 (2020).
- 28 B. Lauss and B. Blau, “UCN, the ultracold neutron source—Neutrons for particle physics,” *SciPost Phys. Proc.* **5**, 4 (2021).

- <sup>29</sup>M. Demper and N. Volbers, “Nickel-iron alloys (NiFe): An overview of the NiFe alloys for sensor applications,” in *UK Magnetics Society MagNews* (2015).
- <sup>30</sup>QuSpin, Inc. 331 South 104th Street, Suite 130, Louisville, CO 80027, USA.
- <sup>31</sup>F. Thiel, A. Schnabel, S. Knappe-Grüneberg, D. Stollfuss, and M. Burghoff, “Demagnetization of magnetically shielded rooms,” *Rev. Sci. Instrum.* **78**, 035106 (2007).
- <sup>32</sup>J. Voigt, S. Knappe-Grüneberg, A. Schnabel, R. Körber, and M. Burghoff, “Measures to reduce the residual field and field gradient inside a magnetically shielded room by a factor of more than 10,” *Metrol. Meas. Syst.* **20**, 239–248 (2013).
- <sup>33</sup>I. Altarev, P. Fierlinger, T. Lins, M. G. Marino, B. Nießen, G. Petzoldt, M. Reisner, S. Stuiber, M. Sturm, J. Taggart Singh, B. Taubenheim, H. K. Rohrer, and U. Schlöpfer, “Minimizing magnetic fields for precision experiments,” *J. Appl. Phys.* **117**, 233903 (2015).
- <sup>34</sup>Z. Sun, P. Fierlinger, J. Han, L. Li, T. Liu, A. Schnabel, S. Stuiber, and J. Voigt, “Limits of low magnetic field environments in magnetic shields,” *IEEE Trans. Ind. Electron.* **68**, 5385–5395 (2021).
- <sup>35</sup>Bartington Instruments Ltd, Thorney Leys Park, Witney OX28 4GE, United Kingdom, [Bartington.com](http://Bartington.com).